Journal of Colloid and Interface Science 703 (2026) 139141

Contents lists available at ScienceDirect

Journal of Colloid And Interface Science

journal homepage: www.elsevier.com/locate/jcis

Pulsed electrolysis controls sequential accumulation and conversion of key intermediates over zinc-based metal organic framework for enhanced nitrate electroreduction to ammonia

Xi Chen [a], Yuan Liang [b,c], Lin Zhou [a], Fasheng Chen [a], Junjie Ding [d], Mengjun Wang [a], Liyun Zhang [a], Jian Su [b,c,*], Zhong Jin [b,**], Minghang Jiang [a,b,**]

[a] Department of Chemistry, School of Science, Xihua University, Chengdu, Sichuan 610039, PR China
[b] State Key Laboratory of Coordination Chemistry, MOE Key Laboratory of Mesoscopic Chemistry, MOE Key Laboratory of High Performance Polymer Materials and Technology, Jiangsu Key Laboratory of Advanced Organic Materials, Suzhou Key Laboratory of Green Intelligent Manufacturing of New Energy Materials and Devices, Tianchang New Materials and Energy Technologies Research Center, Institute of Green Chemistry and Engineering, School of Chemistry and Chemical Engineering, Nanjing University, Nanjing, Jiangsu 210023, PR China
[c] School of Chemistry and Chemical Engineering, Nanjing University of Science and Technology, Nanjing, Jiangsu 210094, PR China
[d] College of Physics and Center of Quantum Materials and Devices, Chongqing University, Chongqing 401331, China

GRAPHICAL ABSTRACT

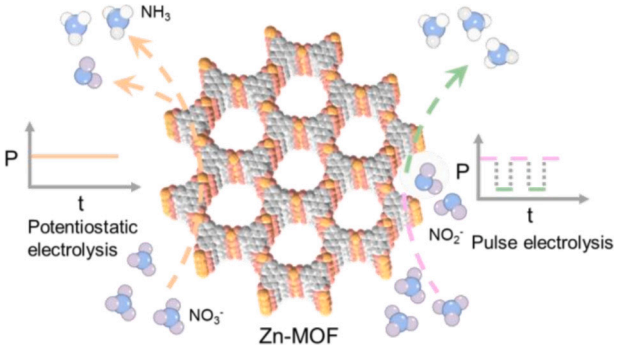

ARTICLE INFO

Keywords:
Pulesd electeocatalysis
Controlling accumulation and conversition of intermidiates
Metal-organic framework

ABSTRACT

The electrochemical nitrate reduction reaction (NO_3RR) to ammonia offers a promising approach for wastewater treatment and ammonia synthesis. However, the generation of various by-products, such as nitrite ions (NO_2^-), and the occurrence of the competitive hydrogen evolution reaction (HER) complicate reaction pathways, causing unwanted electrical energy consumption and reducing the product selectivity. Herein, we introduce a pulse electrolysis approach to control the sequential accumulation and conversion of NO_2^- intermediates during the

* Corresponding author at: State Key Laboratory of Coordination Chemistry, MOE Key Laboratory of Mesoscopic Chemistry, MOE Key Laboratory of High Performance Polymer Materials and Technology, Jiangsu Key Laboratory of Advanced Organic Materials, Suzhou Key Laboratory of Green Intelligent Manufacturing of New Energy Materials and Devices, Tianchang New Materials and Energy Technologies Research Center, Institute of Green Chemistry and Engineering, School of Chemistry and Chemical Engineering, Nanjing University, Nanjing, Jiangsu 210023, PR China.
** Corresponding authors at: Department of Chemistry, School of Science, Xihua University, Chengdu, Sichuan 610039, PR China.
E-mail addresses: sujian@njust.edu.cn (J. Su), zhongjin@nju.edu.cn (Z. Jin), minghang@mail.xhu.edu.cn (M. Jiang).

https://doi.org/10.1016/j.jcis.2025.139141
Received 9 August 2025; Received in revised form 26 September 2025; Accepted 28 September 2025
Available online 30 September 2025

Ammina synthesis
Electrocatalytic nitrate reduction

NO_3RR using a conductive rod-like zinc-based metal organic framework (Zn-MOF) electrode with precise atomic structures. This strategy substantially improves both the yield and Faraday efficiency (FE_{NH3}) of NH_3 production relative to constant-potential electrolysis. After a long-term stability test, the high-purity ammonia product in the electrolyte was successfully extracted *via* an argon (Ar) stripping process, showing a practical way to turn wastewater nitrate into valuable ammonia-derived products. This study presents a promising strategy for rationally designing metal organic framework (MOFs) electro-catalysts with precise atomic structures and controlling complex reactions, thereby minimizing side reactions, significantly boosting nitrate-to-ammonia conversion efficiency.

1. Introduction

Ammonia (NH_3) functions as a vital chemical raw material, boasting broad-spectrum application in fertilizer manufacturing and chemical industry, which is deeply intertwined with human existence and the sustainable advancement of contemporary society [1–3]. Currently, industrial production of NH_3 predominantly relies on the Haber–Bosch (H–B) process under conditions of high temperature and high pressure, emitting huge amount of carbon dioxide [4–7]. To achieve the carbon-neutrality objective and mitigate the global energy crisis, there is an urgent need to develop a green and low-carbon electrochemical method for NH_3 production. Compared with nitrogen (N_2), nitrate (NO_3^-) as a promising nitrogen source for NH_3 synthesis, attributing to their lower N═O bond energy (204 kJ/mol) and excellent solubility characteristics of NO_3^- [8–10]. Moreover, the extensive application of NO_3^- has resulted in substantial contamination of surface water bodies and underground aquifers, thereby presenting a considerable danger to both human wellbeing and the survival of aquatic organisms [11,12]. As a result, the electrochemical nitrate reduction reaction (NO_3RR) stands out as an exceptionally promising approach. It not only helps mitigate environmental pollution but also enables the simultaneous production of valuable NH_3.

The electrochemical NO_3RR aimed at NH_3 synthesis involves a multi-electron/proton transfer process, which is characterized by sluggish kinetics [6,13–15]. Previous studies reported that the absorbed NO_3^- undergoes deoxygenation through two-electron transfer process, resulting in the formation of nitrite (NO_2^-) [16]. This step is widely regarded as the rate-determining step in most catalyst systems leading to massively accumulated NO_2^- around the cathode at low overpotential [17,18]. The massively buildup of NO_2^- intermediate by-products within electrolytes not only reduces the efficiency of converting NO_3^- to NH_3 but also poses challenges for practical water treatment applications [19,20]. Effectively further reducing NO_2^-, which is generated during the reduction process of NO_3^-, to the target product NH_3 is of paramount importance for advancing the development of electrochemical NO_3RR technology. At present, there is indeed a scarcity of research work reporting on this aspect. Previous study revealed that high overpotentials are conducive to the further reduction of NO_2^- intermediate to NH_3 [21,22]. However, under high-overpotential testing conditions, the competitive hydrogen evolution reaction (HER) intensifies its competition for available active sites, thereby causing a drop in the FE_{NH3} [17,23]. Moreover, during prolonged high-overpotential testing, the catalyst structure may sustain damage, which in turn leads to a decrease in its stability [24]. Currently, the majority of electrochemical NO_3RR studies that have been documented so far have centered on constant-potential operation [18]. Compared to traditional constant-potential electrolysis (CPE), the pulsed electrolysis (PE) mode with alternating high/low overpotential periods accelerates key intermediate reduction and product desorption, boosting target product selectivity [25,26]. Recently, PE has garnered substantial interest across a wide range of fields centered around the electrocatalytic conversion of small molecules including carbon dioxide reduction reaction (CO_2RR) [27–29] and oxygen reduction reaction (ORR) [30,31] and so on. However, research on the application of PE in electrochemical NO_3RR remains scarce [17,32].

In addition, the rational design of catalysts holds paramount importance in enhancing the performance of the NO_3RR. Zn is expected to be the most suitable low-cost metal for the conversion of small molecules (*e.g.*, carbon dioxide), given that it demonstrates binding energy comparable to that of precious metals like Au and Ag [33,34]. Moreover, Han et al. demonstrated that Zn doping can modulate the adsorption strength of reaction intermediates, enhance $*NO_2$ conversion efficiency, alter the *NO adsorption configuration from a terminal to a bridge adsorption mode, and reduce the energy barrier, thereby achieving superior catalytic performance for the NO_3^--to-NH_3 conversion [35]. Meanwhile, Zn is distinguished by its lower electronegativity and fully occupied orbitals, which endow it with a diminished capacity to bind H-protons. Consequently, this property makes it conducive to minimizing competition from the HER [36,37]. Unfortunately, as far as we are aware, the experimental implementation of Zn-based electrocatalysts for the NO_3RR has not yet been reported. On the other hand, the porous framework structure and uniformly dispersed metal centers characteristic of metal organic framework (MOFs) offer significant structural advantages for enhancing the performance of the NO_3RR. However, due to the inherently poor electrical conductivity of MOFs, they must be transformed into carbon skeleton materials through high-temperature calcination to enhance their conductivity [21,38]. Nevertheless, high-temperature pyrolysis treatment tends to disrupt the microstructure of the support material, leading to issues such as metal atom agglomeration and complexities in the preparation process. Based on the aforementioned analysis, the rational design of conductive Zn-based MOFs electrocatalysts with precise atomic structures holds significant implications for expanding the selection of catalyst materials and optimizing their structural designs in the field of electrochemical NO_3RR.

Herein, we synthesized a conductive rod-shaped zinc-based metal organic framework (Zn-MOF) electrode with precise atomic architectures *via* hydrothermal method. A pulse electrolysis strategy was proposed to control NO_2^- intermediate accumulation and conversion near the electrode during NO_3RR. Consequently, it leads to a substantial enhancement in both the NH_3 yield and Faraday efficiency (FE_{NH3}) when compared with traditional constant−potential electrolysis mode. Specifically, in the electrochemical NO_3RR system, pulsed conditions ($E_L = -0.6$ V, $E_H = -1.1$ V *vs* standard reversible hydrogen electrosde (RHE), $t_L = t_H = 5$ s) doubled both NH_3 yield and FE_{NH3} compared to constant-potential operation at −1.1 V *vs* RHE. Moreover, in a flow−cell setup, the Zn-MOF catalyst achieved a high current density (>180 mA cm^{-2} at −1.1 V *vs* RHE) and demonstrated excellent stability over successive cyclic and long-duration tests, with high-purity solid NH_4Cl efficiently extracted *via* argon (Ar) stripping post-test. This study provides insights for designing Zn-based electrocatalysts with precise atomic structures, employing a pulse electrolysis mode to optimize NO_2^- intermediate accumulation and achieve highly selective NO_3^- electroreduction to NH_3.

2. Experimental section

2.1. Chemicals and materials

Zinc acetate dihydrate ($C_4H_{10}O_6Zn$, 99 %) and isopropanol (C_3H_8O, 99.9 %) were obtained from Aladdin. Hexahydroxytriphenylene (HHTP,

99 %) was purchased from Adamas. Sodium hydroxide (NaOH, 95 %), p-aminobenzenesulfonic acid ($C_6H_7NO_3S$, 99.5 %), p-dimethylaminobenzaldehyde ($C_9H_{11}NO$, 99 %), sodium nitroprusside dihydrate ($C_5H_2FeN_6NaO_2{\cdot}2H_2O$, 99 %) and N-(1-naphthyl) ethylenediamine dihydrochloride ($C_{12}H_{14}N_2{\cdot}2HCl$, 98 %) were purchased from Macklin. KNO_3 (99 %), anhydrous ethanol (C_2H_5OH, 99.7%), concentrated hydrochloric acid (HCl, 99 %), and sodium sulfate (Na_2SO_4, 99.5 %) were sourced from Kelong. All chemicals were utilized in their as-received state, without any additional purification steps. The water used as a reagent in all experimental procedures was deionized water.

2.2. Synthesis of conductive Zn-MOF sample

The conductive rod-like Zn-MOF was synthesized through a hydrothermal method. Specifically, 0.05 mmol of $C_4H_{10}O_6Zn$ was dissolved in 5 mL of deionized water, resulting in the formation of a homogeneous metal salt solution. Subsequently, the metal salt solution was added drop by drop to a 5 mL isopropanol dispersion that contained 0.3 mmol of HHTP, followed by magnetic stirring for 15 min. After that, the resulting mixture was transferred to a Teflon-lined stainless autoclave and reacts at 85 °C for 15 h. After the mixture was cooled to room temperature, the obtained precipitate was rinsed with water and ethanol and then vacuum dried at 50 °C.

2.3. Material characterizations

Powder X-ray diffraction (XRD) analysis was carried out on a Haoyuan DX-2800, scanning from 2 to 30° at a scanning rate of 2° min^{-1}. The surface morphology and structural features were comprehensively investigated utilizing a field-emission scanning electron microscope (SEM, FEI Nova NanoSEM 450) and a transmission electron microscope (TEM, JEM-2100F). The surface element compositions and detailed valence states of all samples were determined by X-ray photoelectron spectroscopy (XPS) on a Thermo Scientific K-Alpha instrument. The ultraviolet-visible absorption spectrum (UV-Vis) absorbance spectra were measured on a Shimadzu UV-2700 instrument. The liquid product was measured by nuclear magnetic resonance spectroscopy (NMR, Bruker AV-400). The products were analyzed by using Fourier transform infrared spectroscopy (FTIR, Thermo Scientific Nicolet IS 10).

2.4. Electrochemical measurements

Electrochemical measurements were carried on a Chenhua CHI-760E electrochemical workstation in an H-type electrolytic cell separated by a Nafion-117 proton exchange membrane. A piece of carbon paper (CP, 1 × 1 cm^2) coated with the as-prepared electrocatalyst (areal loading: 0.4 $mg{\cdot}cm^{-2}$), a Pt disk electrode (1 × 1 cm^2) and a standard Ag/AgCl electrode were used as the working, counter and reference electrode, respectively. The proton exchange membrane was respectively treated in H_2O_2 (5 %) aqueous solution, deionized H_2O, and 0.5 M H_2SO_4 for 1 h at 80 °C before starting the electrochemical test. All potentials in this experiment were calibrated to reversible hydrogen electrode (RHE) by using the eq. E (*vs* RHE) = E (*vs* Ag/AgCl) + 0.1989 + 0.059 × pH. In this study, all electrochemical measurements were carried out at room temperature.

2.5. Calculations of the NH_3 yield and the faradaic efficiency for NH_3 (FE_{NH3})

The NH_3 yield (Y_{NH3}) can be calculated as: Y_{NH3} (μg $h^{-1}mg_{cat.}^{-1}$) = (C_{NH3} × V)/(t × $m_{cat.}$), where C_{NH3} (μg mL^{-1}) is the measured NH_3 concentration, V (mL) is the volume of the electrolyte, t (h) is the reaction time, and m (mg) is the catalyst loading mass on the CP. The FE_{NH3} can be calculated as: FE_{NH3} = (n × F × C_{NH3} × V)/(17 × Q), where n is the number of transferred electrons, F is the Faraday constant (96,485C mol^{-1}) and Q (C) is the total amount of applied electricity.

2.6. In-situ IR measurement

In situ infrared spectrum (*in-situ* IR) was performed in an *in-situ* IR spectrometer system (Shimadzu, IRTracer100) with a mercury cadmium telluride detector. A customized H-type electrochemical cell, outfitted with an Ag/AgCl reference electrode, a graphite rod counter electrode, and a working electrode, served as the *in-situ* IR electrochemical cell for our experiments. For the preparation of the working electrode, 20 μL of catalyst ink was drop-coated onto the surface of the working electrode. The spectra were collected at the potential range of −0.9 to −1.3 V *vs* RHE.

3. Results and discussions

3.1. Preparation and characterizations of samples

As depicted in Fig. 1a, the zinc-based metal organic framework (Zn-MOF) was synthesized through a hydrothermal process, employing Zn^{2+} centers as the inorganic node and hexahydroxytriphenylene (HHTP) as the organic linker. Specifically, in the solvothermal reaction, the Zn^{2+} ions bonded with oxygen atoms derived from the HHTP ligands, thereby forming a parallel building unit. After undergoing crystal growth at a temperature of 85 °C for a duration of 15 h, the Zn-MOF was obtained. At the beginning, field-emission scanning electron microscopy (SEM) was conducted to observe the surface morphology of Zn-MOF sample (Fig. 1b and c), which was clearly displayed that obtained sample possesses regular rod shape with the length over 20 μm. The corresponding elemental mappings of the Zn-MOF (Fig. 1d–f) revealed a homogeneous distribution of Zn and C elements across the entire rod-shaped MOF matrix. This demonstrated that Zn ions coordinated with HHTP to form a uniform MOF structure. Moreover, the microstructures of the Zn-MOF sample were examined using field-emission transmission electron microscopy (TEM). As depicted in Fig. 1g and h, a distinct crystalline lattice structure within the Zn-MOF was observed. This structure displayed an interplanar spacing of 2.0 nm corresponding to the (1 0 0) crystallographic plane, as illustrated in the inset of Fig. 1h. Such an ordered arrangement served as compelling evidence of the material's high level of structural regularity and the successful accomplishment of its synthesis.

Powder X-ray diffraction (XRD) was employed to investigate the structure details of the samples. As illustrated in Fig. 2a, when compared with pristine HHTP, the Zn-MOF sample exhibited distinct diffraction peaks. This observation implied that Zn^{2+} ions have successfully coordinated with the organic ligands, resulting in the formation of the Zn-MOF structure (Fig. 2b). The diffraction peaks of Zn-MOF at 4.7°, 9.6°, 12.6° and 27° could be correspond to (1 0 0), (2 0 0), (2 1 0), and (1 1 2) planes (Fig. 2a). The aforementioned analysis results align with the observations from TEM, indicating the successful preparation of the Zn-MOF sample. Subsequently, Fourier transform infrared (FTIR) spectroscopy and X-ray photoelectron spectroscopy (XPS) were implemented to further investigate the chemical bond and chemical state of Zn-MOF sample. The FTIR spectra shown in Fig. 2c revealed a notable decrease in the intensities of characteristic vibrational peaks associated with the —OH group at 3440 cm^{-1} and the C—OH group at 1124 cm^{-1} within the Zn-MOF framework, when compared to pristine HHTP. This attenuation can be attributed to the coordination of Zn^{2+} ions with the oxygen atoms of the HHTP ligands during the formation of the Zn-MOF. Furthermore, the peak observed at 1602 cm^{-1} was attributed to the C═O stretching vibration. This indicated the occurrence of *in-situ* oxidation of the HHTP ligands, as shown in Fig. 2d. An analysis of the surface compositions and valence states of the samples was conducted *via* XPS. Fig. 2e showed the XPS survey spectra of Zn-MOF and HHTP samples. The high-resolution C 1s spectra of both Zn-MOF and HHTP can be deconvoluted into three distinct peaks, which corresponding to C—C (284.80 eV), C—O (286.25 eV), and C═O (287.92 eV) bonds, respectively (Fig. 2f). In the high-resolution XPS spectra within the O 1s region for both the Zn-MOF

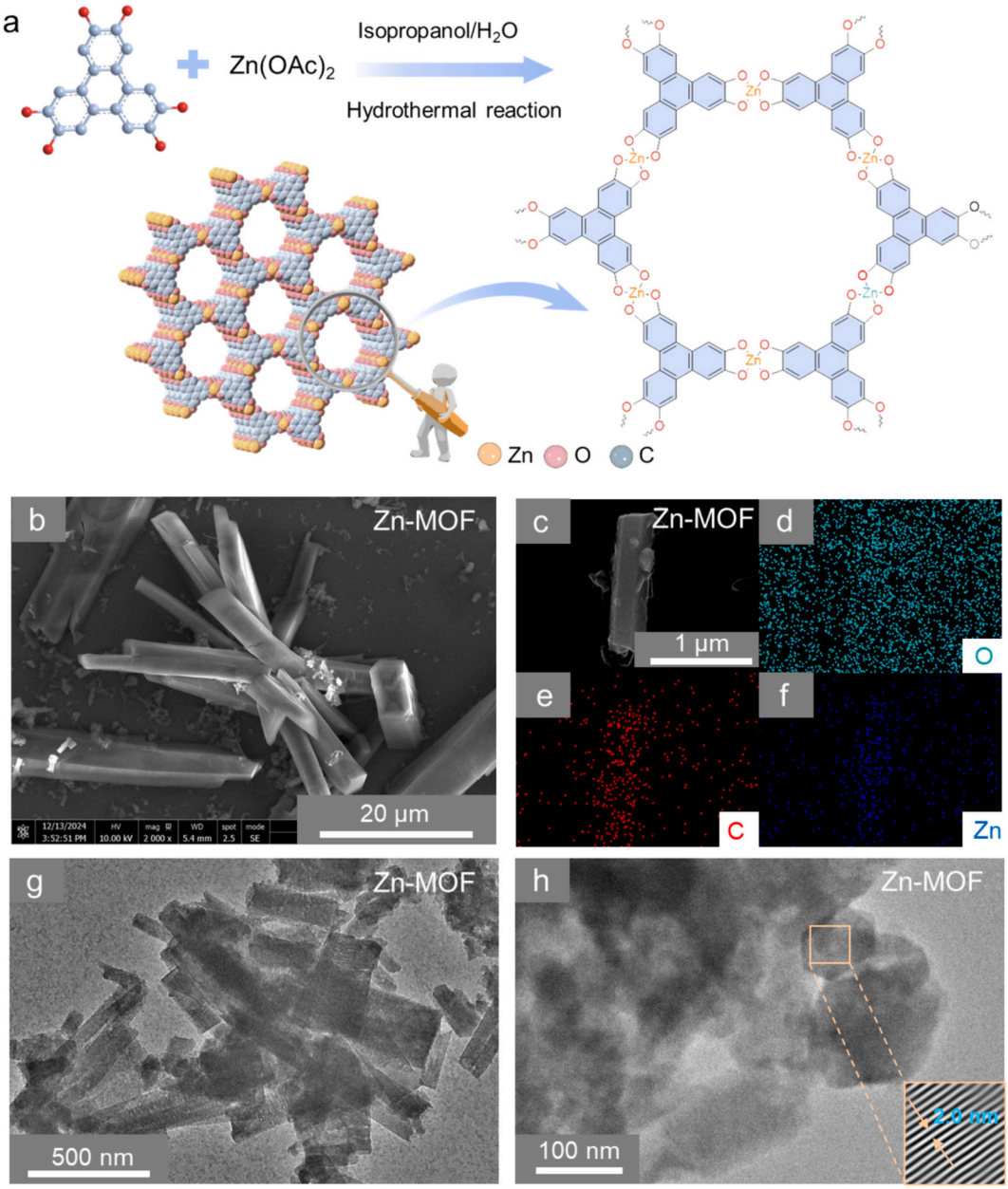

Fig. 1. Schematic illustration of the synthesis process, along with morphological and structural analysis of the samples. (a) Schematic illustration of Zn-MOF sample synthesis. (b, c) SEM, (d–f) element mapping images, (g) TEM and (h) HR-TEM images of Zn-MOF sample.

and HHTP samples (Fig. 2g), characteristic signals corresponding to the C—O (532.05 eV) and C═O (533.25 eV) bonds were detected in both materials. The aforementioned fitting outcomes confirm that HHTP underwent an *in-situ* oxidation process, resulting in the formation of C═O species. This observation was consistent with the FTIR experimental findings. Moreover, the Zn-MOF sample displayed an additional fitting peak at 530.60 eV in the O 1s spectrum, which can be attributed to the Zn—O—C bond. Moreover, as shown in Fig. 2h, the Zn—O bond, identified at a binding energy of 1022.89 eV, was exclusively observed in the XPS spectrum at the Zn 2p region of Zn-MOF. This observation suggested the formation of the desired Zn-MOF structure (Fig. 1a).

3.2. Electrocatalytic nitrate and nitrite reduction performances

The electrochemical nitrate reduction reaction (NO_3RR) performance of Zn-MOF catalyst was systematically investigated under ambient condition in a standardized three-electrode electrochemical cell configuration, incorporating Nafion-117 proton-conductive membrane as separator (Fig. S1). Initially, we conducted constant-potential electrolysis (CPE) test to investigate the electrocatalytic NO_3RR performance of Zn-MOF (Fig. 3a). According to linear sweep voltammetry (LSV) curves, compared with 0.1 M Na_2SO_4 electrolyte, Zn-MOF showed more higher negative current densities in 0.1 M Na_2SO_4 and 500 ppm nitrate (NO_3^-) electrolyte (Fig. 3b), indicating the possible occurrence of NO_3RR. To further explore the catalytic performance of the Zn-MOF, NO_3RR tests were conducted under constant-potential conditions, spanning a potential range from −0.9 V to −1.3 V *vs* standard reversible hydrogen electrode (RHE) (Fig. S2). Following the implementation of 30-min chronoamperometry (CA) measurements conducted within a potential window ranging from −0.9 V to −1.3 V *vs* RHE in a 0.1 M Na_2SO_4 with 500 ppm NO_3^- solution, the potential ammonia (NH_3) product in the electrolyte solution within the cathode chamber was quantitatively analyzed utilizing the indophenol blue method (Fig. S3 and S4). Fig. S4a illustrated the UV–vis absorption spectra of standard

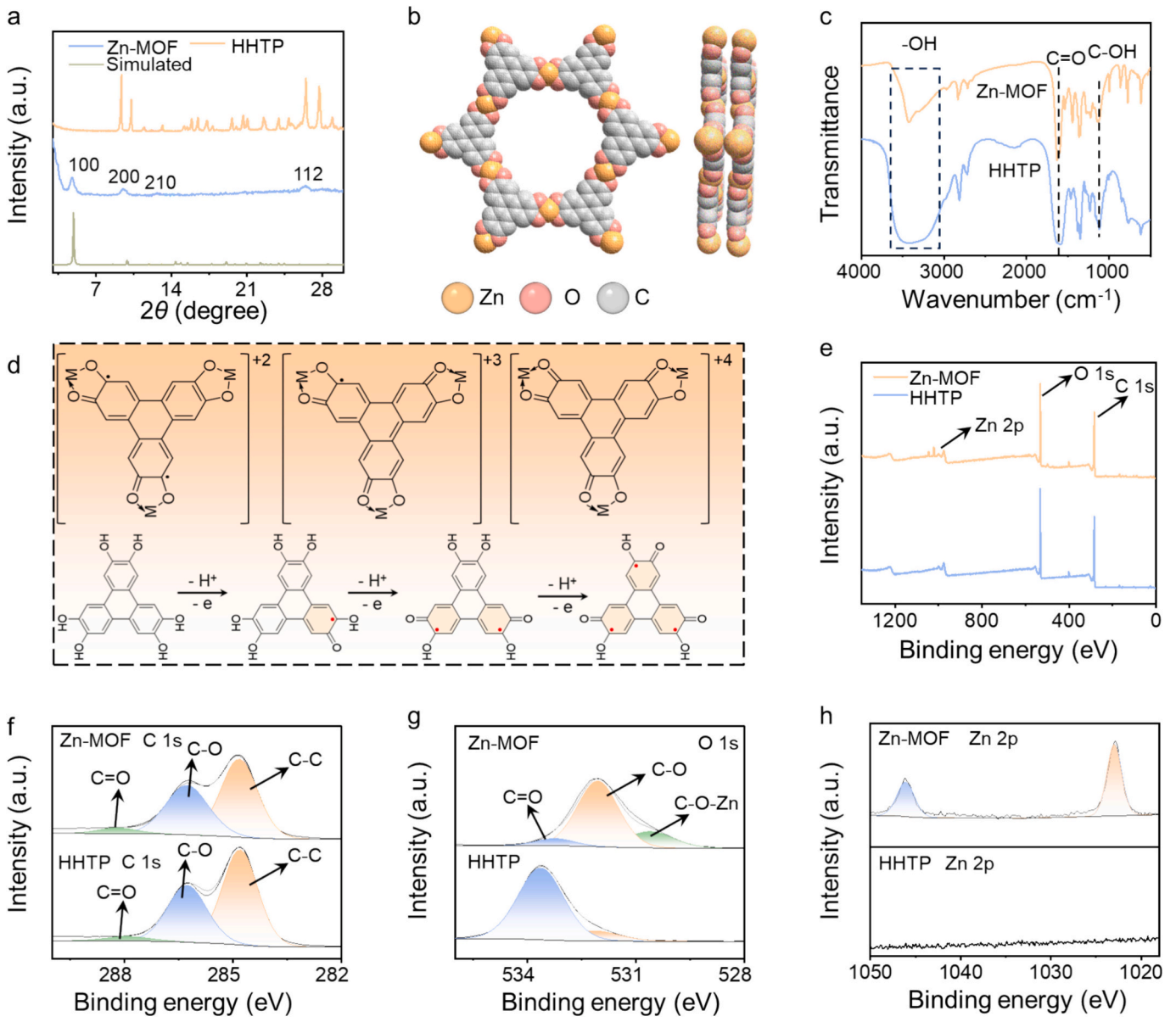

Fig. 2. Spectroscopic analyses. (a) XRD patterns of Zn-MOF and HHTP. (b) The atomic structure model of Zn-MOF. (c) Infrared spectra of Zn-MOF and HHTP samples. (d) Lewis structures of the $HHTP^{6-}$ structures, revealing the charge states and spin structures of the $HHTP^{n-}$. (e) Survey XPS profiles of Zn-MOF and HHTP samples. (f-h) High-resolution XPS spectra at the (f) C 1s, (g) O 1s and (h) Zn 2p region of Zn-MOF and HHTP.

NH_3 solutions with different concentrations, while Fig. S4b presented the associated calibration curves. Fig. S4b demonstrated a remarkably good linear correlation between the light absorbance measured at a wavelength of 655 nm and the concentration of NH_3. By employing the NH_3 standard curve calibration shown in Fig. S4b, the NH_3 yield and the corresponding FE_{NH_3} values (Fig. 3c) for the Zn-MOF catalyst was calculated at various constant-potential conditions. The resulting Zn-MOF exhibited a NH_3 yield of 165.6 μmol h^{-1} $mg_{cat.}^{-1}$ and a Faraday efficiency of NO_3^- (FE_{NH3}) of 57.7 % at −1.2 V *vs* RHE, were obviously higher than that of pristine HHTP (21.7 μmol h^{-1} $mg_{cat.}^{-1}$ and 9.8 %, respectively) (Fig. 3d). This phenomenon demonstrated that Zn species served as the primary active site within the metal organic framework (MOFs) structure. Additionally, the presence of by-product nitrite (NO_2^-) in the Zn-MOF electrolyte solution was ascertained using the Griess indicator method (Fig. S5). Fig. S6 demonstrated that as the applied potential increases from −0.7 V to −1.3 V *vs* RHE, the Faraday efficiency of NO_2^- (FE_{NO2}^-) decreased sharply. This trend was likely attributable to the enhanced reduction of NO_2^- to NH_3 under more negative potential. The Zn-MOF sample demonstrated a NO_2^- yield of 801.0 μg·h^{-1}·$mg_{cat.}^{-1}$ and a FE_{NO2-} of 53.7 % at −1.1 V *vs* RHE under constant-potential conditions. This indicated that NO_2^- was the primary byproduct of the NO_3RR under constant-potential test conditions.

Given that applying a more negative potential had facilitated the further conversion of NO_2^- into the desired NH_3 product, yet had simultaneously exacerbated the occurrence of the competitive hydrogen evolution reaction (HER) as a side-reaction, a pulsed electroreduction strategy (Fig. 3a) was introduced to address these challenges. The pulse parameters were set to high potential (E_H) (E_H = −0.9 V, −1.0 V, −1.1 V, −1.2 V and − 1.3 V *vs* RHE, respectively) for t_H (s) followed by low potential (E_L) (E_H = −0.6 V *vs* RHE) for t_L (s) and then the alternating change in potential repeats. As illustrated in Figs. S7–S10, a range of cathodic potentials and pulse periods were applied to further monitor and evaluate their impacts on the performance of the electrochemical NO_3RR for NH_3 synthesis. Taking NH_3 yield and FE_{NH3} as the evaluation metrics, the optimal parameters of E_H = −1.1 V, E_L = −0.6 V, t_H = 5 s, and t_L = 5 s are chosen and employed in the subsequent experiments

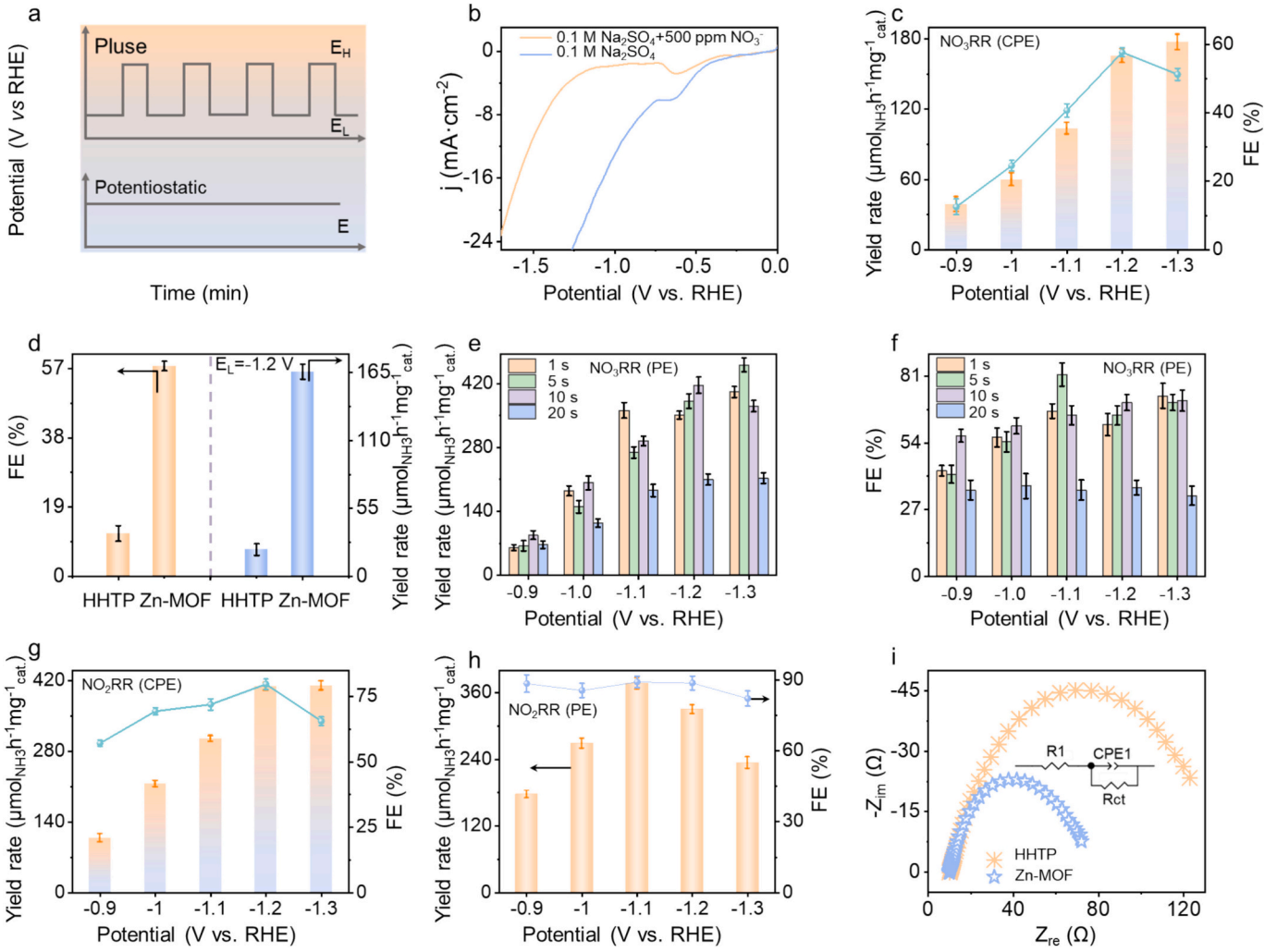

Fig. 3. Electrocatalytic NO_3RR performance of the samples. (a) Schematic illustration of constant-potential and pulsed potential tests. (b) LSV tests were conducted on Zn-MOF in a 0.1 M Na_2SO_4 solution, both with and without the presence of 500 ppm NO_3^-, respectively. (c) The NH_3 yield and corresponding FE_{NH3} for Zn-MOF measured in constant-potential condition for NO_3RR (Error bars are made using the standard deviation of three experiment repeats). (d) The NH_3 yield and corresponding FE_{NH3} at −1.2 V *vs* RHE of HHTP and Zn-MOF measured in constant-potential condition for NO_3RR (Error bars are made using the standard deviation of three experiment repeats). (e) The NH_3 yield and (f) corresponding FE_{NH3} values of Zn-MOF for NO_3RR under pulse conditions (Error bars are made using the standard deviation of three experiment repeats). (g) The NH_3 yield and corresponding FE_{NH3} values of Zn-MOF for NO_2RR under constant-potential conditions (Error bars are made using the standard deviation of three experiment repeats). (h) The NH_3 yields and corresponding FE values for Zn-MOF at given potentials for NO_2RR under pulse conditions (E_L = −0.9 to −1.3 V, E_H = −0.6 V, $t_L = t_H$ = 5 s) (Error bars are made using the standard deviation of three experiment repeats). (i) Nyquist plots of HHTP and Zn-MOF measured at −1.1 V *vs* RHE in 0.1 M Na_2SO_4 solution containing 500 ppm of NO_3^-.

(Fig. 3e and f). In comparison to constant-potential conditions, which exhibited a NH_3 yield of 165.6 μmol h^{-1} $mg^{-1}_{cat.}$ and a FE_{NH3} of 57.7 %, pulsed conditions demonstrated markedly superior performance, achieving an NH_3 yield of 461.1 μmol h^{-1} $mg^{-1}_{cat.}$ and an FE_{NH3} of 80.5 % (Fig. 3e and f). Moreover, the potential byproduct NO_2^- in the 0.1 M Na_2SO_4 and 500 ppm NO_3^- electrolyte under pulsed conditions (E_L = −0.6 V *vs* RHE, E_H = −1.1 V *vs* RHE, $t_L = t_H$ = 5 s) were also detected by Griess indicator method. As shown in Fig. S11, when using Zn − MOF as the cathode, the FE_{NO2-} obtained *via* pulsed electroreduction was significantly lower than that achieved under constant−potential electroreduction (Fig. S6) across the entire applied negative potential window (from −0.7 V to −1.3 V *vs* RHE). This observation suggested that the pulsed electroreduction method promoted the further conversion of the reaction intermediate *NO_2 into the target product, NH_3. The pulse-driven electrolytic mode exhibited superior NO_3RR activity compared to the constant-potential test. This enhanced performance may be attributed to the fact that the periodic application of alternating high and low potentials facilitates the rapid conversion of NO_2^- into NH_3. To further provide evaluate the conversion capability of *NO_2^- intermediate, supplementary control experiments on the electrocatalytic reduction of nitrite (NO_2RR) were carried out utilizing a sulfate solution with nitrite incorporated as the electrolyte (Fig. S12 and S13). Specifically, we utilized a 0.1 M Na_2SO_4 solution containing 500 ppm NO_2^- as the electrolyte. The Zn − MOF catalyst exhibited a remarkable FE_{NH3} of 89.8 % under pulse conditions (E_L = −1.1 V, E_H = −0.6 V, $t_L = t_H$ = 5 s). This efficiency was significantly higher than that achieved when using NO_3^- as the nitrogen source, which only reached 62.1 % at −1.1 V *vs* RHE under constant-potential conditions (Fig. 3g and h). The notable rise in NH_3 selectivity achieved through pulsed electrolysis offered further evidence that employing alternating high and low potentials can substantially enhance the conversion of NO_2^- to NH_3. This method not only minimized the formation of by−products but also improved the overall efficiency of the NO_3RR process in producing NH_3. Furthermore, NO_3RR performance of the Zn-MOF electrocatalyst proved to be exceptionally competitive in comparison with other recently documented electrocatalysts (Table S1). Additionally, the Watt and Chrisp method (Fig. S14) was employed to detect the potential byproduct hydrazine (N_2H_4). Fig. S15 unequivocally indicated the absence of N_2H_4 during the

NO_3RR. These analytical findings suggested that the Zn-MOF sample displayed outstanding selectivity in the electrochemical reduction of NO_3^- to NH_3. To gain a more profound understanding of the factors contributing to the divergent NO_3RR performances exhibited by the samples of Zn-MOF and HHTP, we performed electrochemical impedance spectroscopy (EIS) measurements in 0.1 M Na_2SO_4 solution containing 500 ppm NO_3^-, at an applied potential of −1.1 V *vs* RHE. The results are presented in Fig. 3i, the Nyquist plots for all samples were fitted using a typical equivalent circuit (inset of Fig. 3i) to determine the values of the charge transfer resistance. It was noteworthy that the equivalent series resistance values (R_{ct}) of Zn-MOF (63.53 Ω) was obviously lower HHTP (128.7 Ω), suggesting Zn-MOF possesses higher electron transfer efficiency compared with pristine HHTP. Additionally, the electrochemical active surface area (ECSA) was assessed by measuring the catalyst's electric double-layer capacitances (C_{dl}) (Fig. S16). By linearly plotting the anodic charging currents against the scan rates at the open-circuit potential, we determined the C_{dl} values for Zn-MOF (0.75 mF·cm^{-2}) and HHTP (0.59 mF·cm^{-2}). These findings suggested that Zn-MOF possessed a substantially larger electrochemically active specific surface area, which was advantageous for exposing a greater number of catalytic active sites during the electrocatalytic NO_3RR.

To rule out the possibility of NH_3 being introduced due to external environmental contamination, a series of comparative experiments were carried out at the optimal potential of −1.1 V *vs* RHE (Fig. 4a). Initially, a control experiment was conducted, which involved subjecting the Zn-MOF sample to an electrolysis test in a 0.1 M Na_2SO_4 solution at −1.1 V *vs* RHE. The results of this experiment showed that no detectable NH_3 was generated. Furthermore, an electrolysis test was performed on the Zn-MOF sample in a 0.1 M Na_2SO_4 solution containing 500 ppm NO_3^- at the open-circuit potential (OCP), and no NH_3 was detected. Similarly, when the Zn-MOF electrode was replaced with bare carbon paper (CP) in a 0.1 M Na_2SO_4 solution containing 500 ppm NO_3^- at a potential of −1.1 V *vs* RHE, no NH_3 was generated. Moreover, ^{15}N isotope labeling experiments were performed to clarify the origin of NH_3. In these experiments, $Na^{15}NO_3$ was utilized as the nitrogen source. As illustrated in Fig. 4b, the ^1H NMR spectrum of the electrolyte obtained from 0.5 h chronoamperometry test, displayed distinct double peaks. These peaks can be attribute to $^{15}NH_4^+$, which derived from electroreduction of $Na^{15}NO_3$. Fig. 4b illustrated that when using $^{15}NO_3^-$ as the nitrogen source, typical double-split peaks in the ^1H nuclear magnetic resonance (NMR) spectrum corresponding to $^{15}NH_4^+$ species are detected, while no triplet-split ^1H NMR peaks of $^{14}NH_4^+$ were observed. However, the situation was reversed when $^{14}NO_3^-$ was employed as the nitrogen source.

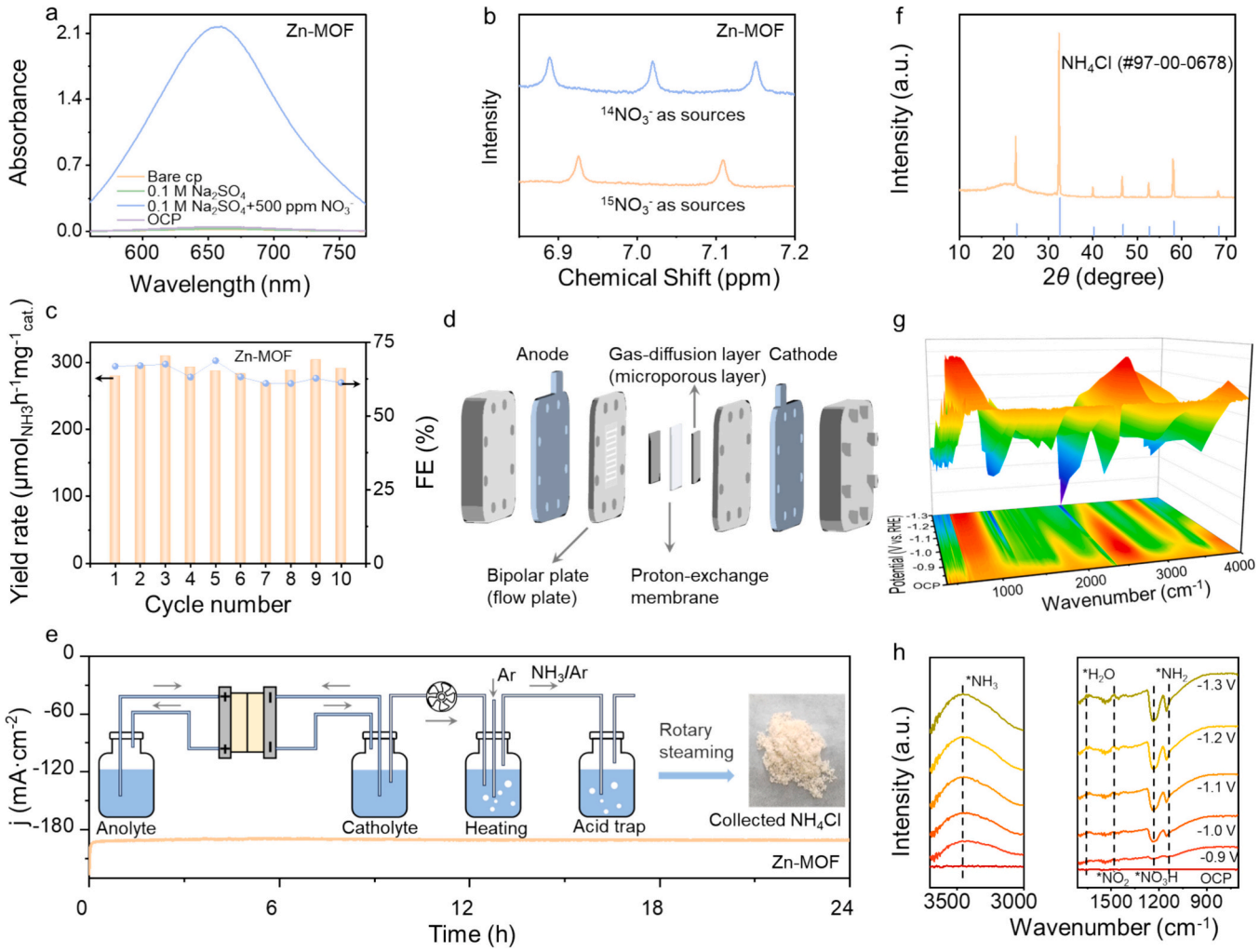

Fig. 4. (a) UV–vis absorption spectra were recorded for the Zn-MOF sample after 10 min of electrolysis under varied conditions, with subsequent colorimetric detection using the indophenol indicator. (b) ^1H NMR spectra were acquired for the electrolyte solutions following nitrogen isotope-labeled NITRR tests on Zn-MOF, using $^{15}NO_3^-$ and $^{14}NO_3^-$ as separate nitrogen sources. (c) Cycling stability of Zn-MOF for the NO_3RR during 10 cycles (E_L = −0.6 V, E_H = −1.1 V *vs* RHE, $t_L = t_H$ = 5 s). (d) Schematic diagram of a flow−type electrolytic cell. (e) I − t curves of Zn-MOF measured in a flow-type electrolytic cell. The inset in Fig. 4e shows the procedure for purifying and collecting the NH_3 product following NO_3RR. (f) XRD pattern for the synthesized NH_4Cl products. (g) and (h) *In-situ* infrared spectra of Zn-MOF sample at different negative applied potentials.

In this case, typical triplet-split ^{1}H NMR peaks of $^{14}NH_4^+$ species were detected, and no double-split ^{1}H NMR peaks of $^{15}NH_4^+$ are observed. These analyses confirmed that the NH_3 present in the product solution stemmed from the electrochemical reduction of NO_3^- on the Zn-MOF catalyst, rather than being introduced from external environmental NH_3 contamination.

Stability stands as a crucial criterion for evaluating the performance of electrocatalysts. Consequently, we investigated the long−term durability of the Zn − MOF sample in a 0.1 M Na_2SO_4 solution that contains 500 ppm of NO_3^-. As depicted in Fig. 4c, the outcomes of 10 successive cyclic tests under pulse conditions ($E_L = -0.6$ V, $E_H = -1.1$ V *vs* RHE, $t_L = t_H = 5$ s) were conducted on the Zn-MOF catalyst, which revealed no significant alteration in either the NH_3 production rate or the FE_{NH3}. This indicated that the NO_3RR performance of the Zn-MOF catalyst remains well-preserved. In addition, an assessment of both the long-term stability and commercial viability of the Zn-MOF sample was carried out in a flow-type electrolytic cell (Figs. 4d and S17). According to Fig. 4e, the catalyst sustained a high current density exceeding 180 mA cm^{-2} at −1.1 V *vs* RHE and demonstrated outstanding stability throughout a 24-h testing period. After a 24-h long-term stability test, the NH_3 product that had dissolved in the electrolyte was extracted through a stripping process. The purification and collection processes were shown in the inset of Fig. 4e. Specifically, after the electrolysis process, a continuous flow of argon (Ar) was bubbled through the electrolyte solution. This stream of Ar acted as a medium to transport the liquid NH_3 from the electrolyte into a 0.1 M HCl solution, facilitating the generation of NH_4Cl. The generation of high−purity NH_4Cl(s) was confirmed by the XRD pattern presented in Fig. 4f. Overall, we showcased a comprehensive process that employed a Zn − MOF catalyst to directly transform nitrate−laden influent into usable NH_3 products.

To gain a more in-depth understanding of the electrochemical NO_3RR process taking place on the Zn-MOF catalyst, *in-situ* Fourier Transform Infrared (*in-situ* FTIR) spectroscopy was employed to detect the possible formation of reaction intermediates on the catalyst's surface. As depicted in Fig. 4g and h, the characteristic peak corresponding to $*NO_3H$ [39] was observed at 1239 cm^{-1}. This indicated that NO_3^- was activated on the catalyst surface, a process that was advantageous for the subsequent deoxygenation reaction. Moreover, a characteristic peak at 1493 cm^{-1} was assigned to $*NO_2^-$, indicating that NO_3^- has been successfully reduced to NO_2^-, which facilitated the subsequent hydrodeoxygenation process involving nitrogen-oxygen active species [40]. Additionally, as the applied potential increasing, the intensity of $*NH_3$ absorption peak located at 3446 cm^{-1} gradually strengthened [37], implying NO_3^- successfully transform to NH_3. Furthermore, prominent peaks at 1154 cm^{-1} was detected which were linked to $*NH_2$ [41]. This suggested that NO_3^- was experienced a continuous deoxidation and hydrogenation reaction path. The proposed reaction pathway proceeds as follows: $*NO_3 \rightarrow *NO_2 \rightarrow *NH_2 \rightarrow *NH_3$. Notably, the absorption peak corresponding to $*H_2O$, situated at 1650 cm^{-1}, revealed that as the magnitude of the applied negative potential increased, the intensity of the signal peak became stronger [41]. This implied that it was beneficial for the adsorption and activation of H_2O molecules to produce active hydrogen. It was worth that active hydrogen played a crucial role in NH_3 synthesis during the NO_3RR process. However, its concentration significantly influenced the FE_{NH_3}. Excessively high concentrations of active hydrogen can trigger vigorous HER side-reactions, thereby causing a decline in FE_{NH3}. On the contrary, when the concentration was too low, it impeded the smooth progress of NH_3 synthesis in the NO_3RR process.

4. Conclusion

In contrast to previous studies that primarily focused on the design of electrocatalysts, our work not only emphasizes catalyst design but also modulates the sequential accumulation and conversion of key intermediates (nitrite ions, $*NO_2^-$) by adjusting the electrolysis mode, thereby significantly enhancing the selectivity of electrochemical nitrate (NO_3^-) reduction to ammonia. Specifically, a conductive rod-shaped zinc-based metal organic framework (Zn-MOF) electrode featuring precise atomic architectures was prepared *via* a hydrothermal method. Moreover, a pulse electrolysis strategy is presented to regulate the step-by-step accumulation and transformation of NO_2^- intermediates in the vicinity of a conductive rod-shaped Zn-MOF electrode, during the nitrate reduction reaction (NO_3RR). As a result, it brings about a one-fold increase in both the NH_3 yield and Faraday efficiency (FE_{NH3}) compared to constant-potential electrolysis. Meanwhile, the FE_{NH3} value for the Zn-MOF catalyst attained 80.5 %, outperforming the previously documented electrocatalysts, including Cu SAGs (78 %) [16], 1-Cu NPs@NDC (71.7 %) [20], and Pd-NDs/Zr-MOF (58.1 %) [7]. Furthermore, in a flow-cell setup, the Zn-MOF catalyst maintained a remarkably high current density, surpassing 180 mA cm^{-2} at −1.1 V *vs* the RHE. It showcased exceptional stability, enduring consecutive cyclic tests and prolonged-duration tests without any significant decline in NO_3RR performance. Following a prolonged stability test, the high-purity solid ammonia product within the electrolyte was effectively extracted through an argon (Ar) stripping procedure. This demonstrates a feasible approach for transforming nitrate in wastewater into valuable ammonia-derived products. *In-situ* Fourier Transform Infrared spectroscopy was utilized to identify the crucial intermediates that formed on the surface of the Zn-MOF catalyst during the electrochemical NO_3RR process. This study offers an important experimental references and inspiration for the subsequent design of conductive MOFs with precise atomic structures and the regulation of crucial electrocatalytic reaction steps through pulsed electroreduction technology.

CRediT authorship contribution statement

Xi Chen: Writing – review & editing, Writing – original draft, Software, Methodology, Investigation, Formal analysis, Data curation. **Yuan Liang:** Formal analysis, Data curation. **Lin Zhou:** Formal analysis, Data curation. **Fasheng Chen:** Formal analysis. **Junjie Ding:** Resources. **Mengjun Wang:** Data curation. **Liyun Zhang:** Formal analysis. **Jian Su:** Writing – review & editing, Resources, Formal analysis. **Zhong Jin:** Writing – review & editing, Visualization, Supervision, Resources, Project administration, Funding acquisition. **Minghang Jiang:** Writing – review & editing, Writing – original draft, Visualization, Supervision, Resources, Project administration, Funding acquisition, Formal analysis, Conceptualization.

Declaration of competing interest

The authors declare that they have no known competing financial interests or personal relationships that could have appeared to influence the work reported in this paper.

Acknowledgements

The authors appreciate the financial support from the Natural Science Foundation of China (22479074, 22475096), the Natural Science Foundation of Sichuan Province (2023NSFSC1074), the Talent Introduction Plan of Xihua University (Z222051), the Equipment Preresearch and Ministry of Education Joint Fund (8091B02052407), the Fundamental Research Program Key Project of Jiangsu Province (BK20253008), the Natural Science Foundation of Jiangsu Province (BK20240400, BK20241236), the Science and Technology Major Project of Jiangsu Province (BG2024013), the Scientific and Technological Achievements Transformation Special Fund of Jiangsu Province (BA2023037), the Academic Degree and Postgraduate Education Reform Project of Jiangsu Province (JGKT24_C001), the Key Core Technology Open Competition Project of Suzhou City (SYG2024122), the Open research fund of Suzhou Laboratory (SZLAB-1308-2024-TS005), and the Chenzhou National Sustainable Development Agenda

Innovation Demonstration Zone Provincial Special Project (2023sfq11).

Appendix A. Supplementary data

Supplementary data to this article can be found online at https://doi.org/10.1016/j.jcis.2025.139141.

Data availability

Data will be made available on request.

References

[1] X. Chen, F. Chen, X. Zhong, J. Ding, H. Wang, L. Dai, X. Ma, H. Wang, C. Wu, X. Li, Y. Xiong, Z. Jin, M. Jiang, Copper nanoclusters featuring fully inorganic anionic ligands for enhanced electrocatalytic nitrate-to-ammonia conversion, J. Energy Chem. 110 (2025) 768–777.

[2] M. Jiang, X. Chen, F. Chen, M. Wang, X. Luo, Y. He, C. Wu, L. Zhang, X. Li, X. Liao, Z. Jiang, Z. Jin, Effective N_2 activation strategies for electrochemical ammonia synthesis, Chem 11 (2025) 102441.

[3] F. Chen, X.-Y. Zhong, J. Ding, X. Chen, X. Liao, Z. Jiang, Y. Xiong, Z. Jin, M. Jiang, Trimesic acid modified copper-cobalt layered double hydroxide nanosheets boost electrocatalytic reduction of nitrate to ammonia, J. Colloid Interface Sci. 701 (2026) 138664.

[4] Y. Li, Z. Lu, L. Zheng, X. Yan, J. Xie, Z. Yu, S. Zhang, F. Jiang, H. Chen, The synergistic catalysis effect on electrochemical nitrate reduction at the dual-function active sites of the heterostructure, Energy Environ. Sci. 17 (2024) 4582–4593.

[5] X. Shi, M. Xie, K. Yang, Y. Niu, H. Ma, Y. Zhu, J. Li, T. Pan, X. Zhou, Y. Cui, Z. Li, Y. Yu, X. Yu, J. Ma, H. Cheng, Synergistic effect of Ni/Ni$(OH)_2$ core-shell catalyst boosts tandem nitrate reduction for ampere-level ammonia production, Angew. Chem. Int. Ed. 63 (2024) e202406750.

[6] X. Ouyang, W. Qiao, Y. Yang, B. Xi, Y. Yu, Y. Wu, J. Fang, P. Li, S. Xiong, Intensifying interfacial reverse hydrogen spillover for boosted electrocatalytic nitrate reduction to ammonia, Angew. Chem. Int. Ed. 64 (2025) e202422585.

[7] M. Jiang, J. Su, X. Song, P. Zhang, M. Zhu, L. Qin, Z. Tie, J.-L. Zuo, Z. Jin, Interfacial reduction nucleation of noble metal nanodots on redox-active metal–organic frameworks for high-efficiency electrocatalytic conversion of nitrate to ammonia, Nano Lett. 22 (2022) 2529–2537.

[8] M. Jiang, L. Han, P. Peng, Y. Hu, Y. Xiong, C. Mi, Z. Tie, Z. Xiang, Z. Jin, Quasi-phthalocyanine conjugated covalent organic frameworks with nitrogen-coordinated transition metal centers for high-efficiency electrocatalytic ammonia synthesis, Nano Lett. 22 (2021) 372–379.

[9] W. He, S. Chandra, T. Quast, S. Varhade, S. Dieckhöfer, J.R.C. Junqueira, H. Gao, S. Seisel, W. Schuhmann, Enhanced nitrate-to-ammonia efficiency over linear assemblies of copper-cobalt nanophases stabilized by redox polymers, Adv. Mater. 35 (2023) 2303050.

[10] Y. Fu, S. Wang, Y. Wang, P. Wei, J. Shao, T. Liu, G. Wang, X. Bao, Enhancing electrochemical nitrate reduction to ammonia over Cu nanosheets via facet tandem catalysis, Angew. Chem. Int. Ed. 62 (2023) e202303327.

[11] W.J. Rogan, M.T. Brady, Drinking water from private wells and risks to children, Pediatrics 123 (2009) e1123–e1137.

[12] H. Xu, Y. Ma, J. Chen, W.-X. Zhang, J. Yang, Electrocatalytic reduction of nitrate–a step towards a sustainable nitrogen cycle, Chem. Soc. Rev. 51 (2022) 2710–2758.

[13] M. Jiang, M. Zhu, J. Ding, H. Wang, Q. Yu, X. Chen, Y. He, M. Wang, X. Luo, C. Wu, L. Zhang, X. Yao, H. Wang, X. Li, X. Liao, Z. Jiang, Z. Jin, Nanocluster-agminated amorphous cobalt nanofilms for highly selective electroreduction of nitrate to ammonia, J. Hazard. Mater. 476 (2024) 134909.

[14] F. Dou, F. Guo, B. Li, K. Zhang, N. Graham, W. Yu, Pulsed electro-catalysis enables effective conversion of low-concentration nitrate to ammonia over Cu_2O@Pd tandem catalyst, J. Hazard. Mater. 472 (2024) 134522.

[15] Y. Li, R. Zhao, Q. Yan, L. Lu, Z. Wu, L. Yu, L. Liu, J. Xi, Quantifying nitrate reduction to ammonia performance on metal foam electrodes, Adv. Funct. Mater. DOI:https://doi.org/10.1002/adfm.202516242.

[16] Y. Liu, J. Wei, Z. Yang, L. Zheng, J. Zhao, Z. Song, Y. Zhou, J. Cheng, J. Meng, Z. Geng, J. Zeng, Efficient tandem electroreduction of nitrate into ammonia through coupling Cu single atoms with adjacent Co_3O_4, Nat. Commun. 15 (2024) 3619.

[17] P. Li, R. Li, Y. Liu, M. Xie, Z. Jin, G. Yu, Pulsed nitrate-to-ammonia electroreduction facilitated by tandem catalysis of nitrite intermediates, J. Am. Chem. Soc. 145 (2023) 6471–6479.

[18] M. Jiang, X. Huang, D. Luo, C. Tian, Z. Jin, Recent breakthroughs in electrocatalytic reduction of nitrogen-oxyanions for environmentally benign ammonia synthesis, Nano Energy 135 (2025) 110683.

[19] M. Lee, E. Shevliakova, C.A. Stock, S. Malyshev, P.C.D. Milly, Prominence of the tropics in the recent rise of global nitrogen pollution, Nat. Commun. 10 (2019) 1437.

[20] J.-H. Kim, Y.J. Kang, K.I. Kim, S.K. Kim, J.-H. Kim, Toxic effects of nitrogenous compounds (ammonia, nitrite, and nitrate) on acute toxicity and antioxidant responses of juvenile olive flounder, paralichthys olivaceus, Environ. Toxicol. Pharmacol. 67 (2019) 73–78.

[21] F. Chen, X. Zhou, H. Wang, X. Liu, Q. Yang, X. Chen, Q. Mu, J. Liu, X. Li, X. Liao, Z. Jiang, Z. Jin, M. Jiang, Bidirectional nitrogen neutralization via coupled electrocatalytic processes of nitrate reduction and hydrazine oxidation, Adv. Funct. Mater. 35 (2025) 2421405.

[22] Q. Yan, R. Zhao, L. Yu, Z. Zhao, L. Liu, J. Xi, Enhancing compatibility of two-step tandem catalytic nitrate reduction to ammonia over p-Cu/Co$(OH)_2$, Adv. Mater. 36 (2024) 2408680.

[23] R. Zhao, Q. Yan, L. Lu, L. Yu, H. Chen, T. Yan, L. Liu, J. Xi, Nitrite-mediated pulsed electrocatalytic nitrate reduction to ammonia over Co@Cu NW with dual active sites, ACS Catal. 14 (2024) 17046–17054.

[24] R. Casebolt, K. Levine, J. Suntivich, T. Hanrath, Pulse check: potential opportunities in pulsed electrochemical CO_2 reduction, Joule 5 (2021) 1987–2026.

[25] S. Han, L. Sun, D. Fan, B. Liu, Pulsed electrosynthesis of glycolic acid through polyethylene terephthalate upcycling over a mesoporous PdCu catalyst, Nat. Commun. 16 (2025) 163426.

[26] R. Zhao, Q. Yan, H. Lin, L. Yu, L. Liu, J. Xi, Dynamic pulse electrocatalysis for efficient and directed reduction of nitrate to ammonia, Chem. Catal. (2025), https://doi.org/10.1016/j.checat.2025.101465.

[27] Z. Li, L. Wang, T. Wang, L. Sun, W. Yang, Steering the dynamics of reaction intermediates and catalyst surface during electrochemical pulsed CO_2 reduction for enhanced C_{2+} selectivity, J. Am. Chem. Soc. 145 (2023) 20655–20664.

[28] K.W. Kimura, R. Casebolt, J. Cimada DaSilva, E. Kauffman, J. Kim, T.A. Dunbar, C. J. Pollock, J. Suntivich, T. Hanrath, Selective electrochemical CO_2 reduction during pulsed potential stems from dynamic interface, ACS Catal. 10 (2020) 8632–8639.

[29] Y. Mao, Q. Mao, H. Yang, Q. Liu, X. Dong, Y. Li, S. Zhou, B. Liu, Dynamically stabilizing oxygen atoms in silver catalyst for highly selective and durable CO_2 reduction reaction, Angew. Chem. Int. Ed. 63 (2024) e202410932.

[30] Y. Ding, W. Zhou, J. Li, J. Wang, L. Xie, X. Meng, J. Gao, F. Sun, G. Zhao, Y. Qin, Revealing the in situ dynamic regulation of the interfacial microenvironment induced by pulsed electrocatalysis in the oxygen reduction reaction, ACS Energy Lett. 8 (2023) 3122–3130.

[31] R. Sun, M. Zhu, J. Chen, L. Yan, L. Bai, J. Ning, Y. Zhong, Y. Hu, Tuning the formation kinetics of *OOH intermediate with hollow bowl-like carbon by pulsed electroreduction for enhanced H_2O_2 production, ACS Nano 19 (2025) 13414–13426.

[32] Y. Huang, C. He, C. Cheng, S. Han, M. He, Y. Wang, N. Meng, B. Zhang, Q. Lu, Y. Yu, Pulsed electroreduction of low-concentration nitrate to ammonia, Nat. Commun. 14 (2023) 7368.

[33] S.T. Guo, Y.W. Du, H. Luo, Z. Zhu, T. Ouyang, Z.Q. Liu, Stabilizing undercoordinated Zn active sites through confinement in CeO_2 nanotubes for efficient electrochemical CO_2 reduction, Angew. Chem. Int. Ed. 63 (2023) e202314099.

[34] M. Jiang, H. Wang, M. Zhu, X. Luo, Y. He, M. Wang, C. Wu, L. Zhang, X. Li, X. Liao, Z. Jiang, Z. Jin, Review on strategies for improving the added value and expanding the scope of CO_2 electroreduction products, Chem. Soc. Rev. 53 (2024) 5149–5189.

[35] L. Wu, J. Feng, L. Zhang, S. Jia, X. Song, Q. Zhu, X. Kang, X. Xing, X. Sun, B. Han, Boosting electrocatalytic nitrate-to-ammonia via tuning of N-intermediate adsorption on a Zn–Cu catalyst, Angew. Chem. Int. Ed. 62 (2023) e202307952.

[36] J.J. Wang, H.T.D. Bui, X. Wang, Z. Lv, H. Hu, S. Kong, Z. Wang, L. Liu, W. Chen, H. Bi, M. Yang, T. Brinck, J. Wang, F. Huang, A copper–zinc cyanamide solid-solution catalyst with tailored surface electrostatic potentials promotes asymmetric N-intermediate adsorption in nitrite electroreduction, J. Am. Chem. Soc. 147 (2025) 8012–8023.

[37] Z. Zhang, Y. Lv, Y. Gu, X. Zhou, B. Tian, A. Zhang, Z. Yang, S. Chen, J. Ma, M. Ding, J.-L. Zuo, Dual Zn_5-NiS_4 sites in a redox-active metal-organic framework enables efficient cascade catalysis for nitrate-to-ammonia conversion, Angew. Chem. Int. Ed. 64 (2025) e202418272.

[38] X. Li, T. Chen, B. Yang, Z. Xiang, Fundamental understanding of electronic structure in FeN_4 site on electrocatalytic activity via dz^2-orbital-driven charge tuning for acidic oxygen reduction, Angew. Chem. Int. Ed. 62 (2023) e202215441.

[39] H. Fu, S. Lu, Y. Xin, S. Xiao, L. Chen, Y. Li, K. Shen, In situ bulk hydrogen intercalation in a mirror−symmetric Ru/WO_{3-x} nanoarray boosts neutral electrocatalytic nitrate reduction to ammonia, Energy Environ. Sci. 18 (2025) 818–830.

[40] X. Su, F. Hong, Y. Fang, Y. Wen, B. Shan, Molecular conjugated−polymer electrode enables rapid proton conduction for electrosynthesis of ammonia from nitrate, Angew. Chem. Int. Ed. 64 (2024) e202422072.

[41] S. Han, H. Li, T. Li, F. Chen, R. Yang, Y. Yu, B. Zhang, Ultralow overpotential nitrate reduction to ammonia via a three−step relay mechanism, Nat. Catal. 6 (2023) 402–414.